J. Fluid Mech. (2008), *vol.* 598, *pp.* 383–392.
doi:10.1017/S0022112007009871 Printed in the United Kingdom

Viscous flows in a muddy seabed induced by a solitary wave

YONG SUNG PARK[1], PHILIP L.-F. LIU[1,2] AND STEPHEN J. CLARK[1]

[1]School of Civil and Environmental Engineering, Cornell University, Ithaca, NY 14853, USA

[2]Institute of Hydrological and Oceanic Sciences, National Central University, Jhongli, Taiwan

(Received 23 September 2007 and in revised form 28 November 2007)

Liu & Chan (*J. Fluid Mech.* vol. 579, 2007, p. 467, hereinafter referred to as LC) derived analytical solutions for the interactions between shallow water waves and a viscous fluid seabed. In this paper we present a set of new experimental data on the solitary-wave-induced flows in a viscous muddy seabed so as to validate LC's theory and the approximations employed. In the experiments a clear silicone fluid was used as the viscous mud and particle image velocimetry was employed to measure the velocity field inside the viscous mud. The shear stress along the bottom of the mud bed and the displacement of the water–mud interface were also deduced from data. Experimental results showed excellent agreement with the theoretical solutions. Additional analyses were performed to show that the ratio of the muddy seabed thickness to the corresponding bottom boundary-layer thickness, $\overline{d}$, plays an important role in characterizing mud flow regimes. When $\overline{d} \leqslant 1$, the vertical profile of the horizontal velocity in the mud bed can be parameterized as a parabola. On the other hand, when $\overline{d} \gg 1$, the velocity profile appears as a plug flow above a thin viscous layer. When $\overline{d} \sim O(1)$, the flow patterns are more complex than the other two regimes and flow reversal can occur inside the viscous mud bed.

1. Introduction

In the nearshore region, where the water depth is relatively shallow in comparison with the wavelength, interactions between propagating water waves and the seabed can be significant. On one hand, the seabed can cause wave energy attenuation and can also influence the direction of wave propagation. On the other hand, water waves can generate deformation and transport of the seabed materials by exerting a pressure field and a shear stress field. Since coastal sediments have a wide range of rheological properties, it is difficult to describe them with a single constitutive model. In recent years, several theoretical models have been suggested for different types of sediments. For example, Liu (1973) and Liu, Park & Lara (2007*b*) examined the effects of wave-induced percolation in seabed with coarse sediments. Other models consider the seabed with finer sediments as elastic (e.g. Foda 1989; Wen & Liu 1995), poro-elastic (e.g. Yamamoto *et al.* 1978), viscous (e.g. Gade 1958; Dalrymple & Liu 1978; Liu & Chan 2007, hereinafter referred to as LC) or visco-elastic (e.g. MacPherson 1980) materials.

In parallel to the theoretical development, efforts have also been made to perform laboratory experiments to validate and extend these theories. For example, Liu & Orfila's (2004) analytical solutions for the boundary-layer flows under a transient

long water wave, including the solitary wave, have been validated experimentally by a set of particle image velocimetry (PIV) experiments (Liu, Park & Cowen 2007*a*). Using the perturbation approach suggested by Liu & Orfila (2004), LC derived a set of Boussinesq-type equations for transient long waves with the effects of a viscous muddy seabed. In their derivation, three major assumptions were made: (i) the mud bed is characterized as a viscous fluid and its viscosity is several orders-of-magnitude higher than that of the water; (ii) the thickness of the mud bed is much less than the characteristic wavelength; and (iii) the displacement of the water–mud interface is negligible.

The primary objective of this paper is to present laboratory data for the solitary-wave-induced flows in a viscous muddy bed so as to validate the theory of LC. Further theoretical investigations on flow characteristics are also to be performed.

In § 2, we review LC's theoretical approach and summarize their analytical solutions. The laboratory experiments using PIV for the case in which the thickness of the mud layer is less than that of the mud bottom boundary layer are described in § 3. Detailed experimental results compared with theoretical solutions and subsequent discussions are presented in § 4. Measured interfacial displacements are compared with theoretical estimations to demonstrate that the displacements are indeed negligible. The role of the relative thickness of the mud bed with respect to the bottom boundary layer, $\overline{d}$, is investigated. The flow reversal observed in Liu *et al.* (2007*a*) within the laminar boundary layer during the decelerating phase of the free-stream velocity also occurs in the boundary layer of the mud bed if the thickness of the muddy seabed is larger than the bottom boundary-layer thickness. Flow profiles for different $\overline{d}$ values are discussed. In addition, bottom shear stress is deduced from the experimental data and compared with the theory. Concluding remarks are given in § 5.

2. Analytical solutions for flows in a viscous mud bed under a solitary wave

Following LC, we denote the surface displacement of a solitary wave as $\zeta'(x', t')$. The solitary wave propagates in a constant water depth h' over a viscous mud bed of thickness d'. The solitary wave is characterized by the wave height H_0', a horizontal length scale l_o', which is related to the width of the solitary wave shape, and the time scale $l_o'/\sqrt{g'h'}$. The following dimensionless variables are then introduced:

$$\left.\begin{aligned} x = x'/l_o', \quad (z, d) = (z', d')/h', \quad t = t'\sqrt{g'h'}/l_o', \quad \zeta = \zeta'/H_0', \\ p = p'/\rho_w' g' H_0', \quad u = u'/\epsilon\sqrt{g'h'}, \quad w = w'\mu/\epsilon\sqrt{g'h'}, \end{aligned}\right\} \tag{2.1}$$

in which p' represents the pressure, u' the horizontal velocity component in the x'-direction, w' the vertical velocity component in the z'-direction with the origin located at the undisturbed free surface, ρ_w' the density of water, and g' the acceleration due to gravity. Two dimensionless parameters have been introduced in the above definitions:

$$\epsilon = H_0'/h', \quad \mu = h'/l_o'. \tag{2.2}$$

Inside the mud bed, additional dimensionless variables are defined:

$$u_m = u_m'/\epsilon\sqrt{g'h'}, \quad w_m = w_m'/\alpha\epsilon\sqrt{g'h'}, \quad \alpha^2 = \frac{\nu_m'}{l_o'\sqrt{g'h'}}. \tag{2.3}$$

With ν_m' being the kinematic viscosity of the mud, α^2 can be viewed as the inverse of a Reynolds number based on the horizontal length scale and the phase speed of the solitary wave. The stretched vertical coordinate and the normalized mud bed

thickness

$$\eta = \frac{z+1}{(\alpha/\mu)}, \quad \overline{d} = \frac{\mu}{\alpha} d = d' \left(\frac{\sqrt{g'h'}}{\nu'_m l'_o} \right)^{1/2}, \tag{2.4}$$

are introduced in the mud bed. We remark here that $\overline{d}$ represents the ratio of the mud bed thickness and the wave-induced boundary-layer thickness in the mud bed.

LC assumed that the viscosity of the mud is several orders-of-magnitude higher than that of the water, thus the flow motions in water associated with solitary waves can be considered essentially irrotational. When the viscous effect is completely ignored, analytical solutions describing a solitary wave are available. For instance, Grimshaw (1971) presented a solution for the free-surface displacement and velocity fields up to $O(\epsilon^2)$. The details of Grimshaw's solutions can also be found in Liu *et al.* (2007*a*).

LC argued that in the viscous mud bed it is the balance among the pressure gradient force imposed by the propagating water wave above, the viscous shear force and the inertia force that governs the fluid motion. Assuming the mud bed thickness is small enough that the pressure is essentially uniform in the vertical direction within the layer, LC derived the leading-order velocity fields as follows:

$$u_m(x, \eta, t) = \gamma \left\{ u_b - \int_0^t \frac{\partial u_b}{\partial \tau} \mathrm{erfc} \left[\frac{\eta + \overline{d}}{\sqrt{4(t-\tau)}} \right] \mathrm{d}\tau \right.$$
$$\left. - \sum_{n=1}^{\infty} (-1)^n \int_0^t \frac{\partial u_b}{\partial \tau} \left[-\mathrm{erfc} \left(\frac{-\eta + (2n-1)\overline{d}}{\sqrt{4(t-\tau)}} \right) + \mathrm{erfc} \left(\frac{\eta + (2n+1)\overline{d}}{\sqrt{4(t-\tau)}} \right) \right] \mathrm{d}\tau \right\}, \tag{2.5}$$

where $\gamma = \rho'_w / \rho'_m$ is the density ratio with ρ'_m being the density of the mud, and u_b the horizontal velocity at the water–mud interface and can be evaluated from existing wave solutions (e.g. Grimshaw 1971). The non-dimensional shear stress along the bottom of the mud bed τ_{mb} can be found by differentiating u_m with respect to η at $\eta = -\overline{d}$:

$$\tau_{mb}(x, t) = \frac{\gamma}{\sqrt{\pi}} \int_0^t \frac{\partial u_b}{\partial \tau} \frac{1}{\sqrt{t-\tau}} \left[1 + 2 \sum_{n=1}^{\infty} (-1)^n \exp \left(-\frac{(n\overline{d})^2}{t-\tau} \right) \right] \mathrm{d}\tau. \tag{2.6}$$

Note that both (2.5) and (2.6) can be readily applied to different kinds of wave loading (e.g. cnodial wave) in shallow water as long as u_b is provided. In the present paper, we shall focus on the case of solitary waves for the sake of experimental simplicity.

3. Experiments

To validate the theories presented in LC, laboratory experiments measuring the velocity fields inside and above the mud bed under solitary waves were carried out in the DeFrees Hydraulics Laboratory at Cornell University.

3.1. *Experimental set-up*

The experiments were conducted in a wave tank (32 m long $\times$ 0.6 m wide $\times$ 0.9 m deep), which is equipped with a piston-type wavemaker and glass sidewalls. A section of the tank about 1 m long was replaced with a clear acrylic basin to hold 1.7 cm deep 'mud' and to allow the delivery of laser light from below. Three acoustic wave gauges (Banner Engineering S18U) were used along with our in-house PIV system. The measurement locations are shown in figure 1. The effects due to the finite length

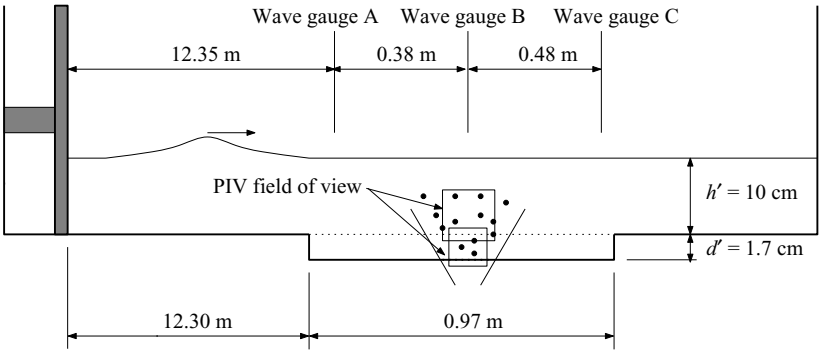

FIGURE 1. Experimental set-up (not to scale).

Wave height H_0' (cm)	Wavelength l_0' (m)	Wave period T' (s)	ϵ	μ	α	$\overline{d}$	Re
0.75	2.62	2.55	0.075	0.038	0.045	0.144	3.33
1.90	1.72	1.59	0.190	0.058	0.056	0.178	3.51
2.90	1.44	1.28	0.290	0.069	0.061	0.195	3.65

TABLE 1. Characteristics of solitary waves generated in the experiments.

of the mud basin were insignificant as the interfacial displacements were negligible and the mud flow was essentially driven by the local horizontal pressure gradient for the cases considered herein (see § 4.2).

A clear silicone fluid (Dow Corning SYLGARD 184 base fluid; $\gamma^{-1} = 1.05$; $\nu_m' = 5.24 \times 10^{-3}\,\mathrm{m^2\,s^{-1}}$ at 25 °C) was chosen as the viscous mud. Gade (1958) reported the values of viscosity and density of top-layer sediments in the Mississippi Delta to be $0.1 < \nu_m' < 1\,\mathrm{m^2\,s^{-1}}$ and $1.6 < \gamma^{-1} < 2.0$, respectively. Consider the experimental case with the wave height $\epsilon = 0.190$, the Reynolds number,

$$Re = \frac{d'\sqrt{g'h'}}{\nu_m'},$$

based on the mud bed thickness and the phase speed of the solitary wave is about 3.51, as shown in table 1. The corresponding field condition, using water depth $h' = 10\,\mathrm{m}$, requires $\nu_m' = 5.36\,\mathrm{m^2\,s^{-1}}$ which is very close to the value by reported Gade (1958).

Three different solitary waves have been studied by changing the wave heights (0.75, 1.90 and 2.90 cm), while the water depth was kept constant, $h' = 10$ cm. The characteristics of the waves generated in the experiments are summarized in table 1, where the wavelength is defined by the width under the wave crest with both ends where the surface displacement is 1.0 % of the wave height. Figure 2(*a*) shows the water-surface profile measured at wave gauge B (above the centre of the PIV measurement region) sampled at 100 Hz for the case with $\epsilon = 0.190$. Grimshaw's higher-order solution (see Liu *et al.* 2007*a*) is also plotted in the same figure. Note that $-\xi = Ct - x$ is a time-like coordinate at a fixed spatial position, say $x = 0$, in figure 2. The agreement between the theoretical results and experimental data is excellent. Similar excellent agreement is also observed for the other two wave conditions, i.e. $\epsilon = 0.075$ and 0.290.

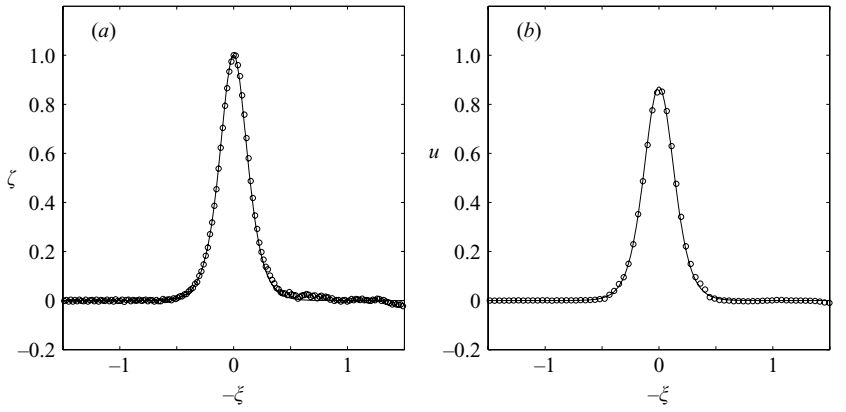

FIGURE 2. (*a*) Theoretical and experimental dimensionless water surface profiles and (*b*) dimensionless horizontal water particle velocities for $\epsilon = 0.190$: ——, Grimshaw's solution; ○, experimental data.

3.2. *PIV analysis procedure*

The PIV technique used here is the same as that employed by Liu *et al.* (2007*a*) which has been shown to be effective in measuring the velocity field inside the laminar bottom boundary layer under a solitary wave. A detailed description of the PIV technique can be found in Liu *et al.* (2007*a*), and here we provide only a brief explanation with numerical values of parameters that are unique to the present experiments.

Two field-of-views (FOV), which were illuminated with a Spectra Physics PIV400-30 Nd:YAG laser system (300 mJ pulse^{-1}, 60 Hz dual head system), were chosen to capture images inside as well as above the mud layer (see figure 1). By passing the laser beam through a cylindrical lens, a light sheet was formed, which was delivered from below the mud basin to avoid disturbances from the free surface. Since the refractive index of the silicone fluid is different from that of the water, the two square FOVs had different side lengths: 24.6 mm in the mud and 29 mm in the water, respectively. The FOV was set parallel to the sidewalls and slightly off the tank centreline to increase image magnification. The distance between the FOV and the nearest sidewall was about 20 cm, which is larger than the boundary-layer thickness of the mud associated with the solitary waves used in the experiments, and the effects of the sidewall are not significant. For each experiment measured inside the mud layer, 105 images were collected with an SMD 1M60-20 camera (12 bits pixel^{-1}, 60 Hz, 1024×1024 pixels) at 15 Hz, yielding 104 velocity field data items at the same rate from the successive cross-correlation analyses of two neighbouring images. A rectangular interrogation subwindow with the long dimension in the horizontal was used (256×16 pixels with 75 % overlap), which yielded 13 subwindows in the horizontal, and 178 in the vertical (1.5 mm horizontal and 0.1 mm vertical resolution inside the mud). Spurious vectors were flagged using an adaptive Gaussian window filter suggested in Liu *et al.* (2007*a*). The filter rejected less than 10 % of the returned data and no attempt was made to smooth or interpolate the original data at this point. On the other hand, the same values of parameters as used by Liu *et al.* (2007*a*) were applied to acquire and analyse the images of the water region.

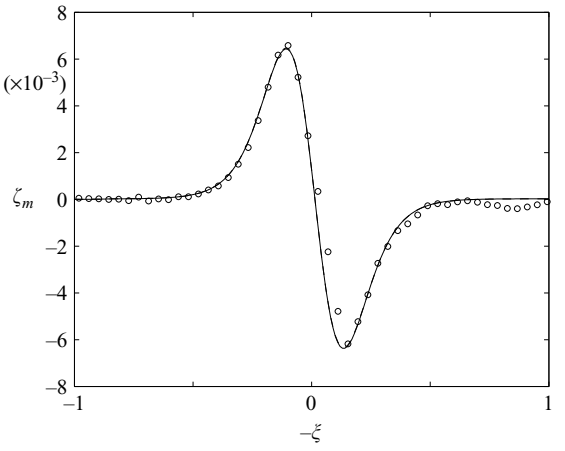

FIGURE 3. Time histories of the dimensionless interfacial displacement for $\epsilon = 0.19$; ——, the analytical solution; ○, the experimental data.

4. Experimental measurements and theoretical results

4.1. *Water particle velocity in the water region*

Some of the laser light was scattered as it passed through the water–mud interface, which caused saturation near the interface in the images taken from the upper FOV. Thus, the velocity data inside the interfacial boundary layer could not be extracted. However, the saturation did not occur far above the interface and the measurements of the free-stream velocity were made. The data is sufficient for the present purpose, as the water is essentially inviscid and our focus is on the velocity field inside the mud layer.

Figure 2(*b*) shows an example of the measured water particle velocity components in the horizontal direction compared with Grimshaw's solution for the case with $\epsilon = 0.190$. In plotting the PIV data, horizontal homogeneity is assumed and the PIV data are averaged along the horizontal direction within the FOV. Good agreement is observed and this, together with the water-surface profile measurements (e.g. figure 2*a*), demonstrate the high quality of the experimentally generated solitary waves. The same is true for the other two cases, namely $\epsilon = 0.075$ and $\epsilon = 0.290$.

4.2. *The displacement of the water–mud interface*

LC assumed that the water–mud interface displacement ζ_m' is negligible, which must be confirmed. Experimentally, the interfacial displacements are obtained by the following procedure. Assuming the locations of the interface are uniform in each image (1024 × 1024 pixels), a Gaussian curve is fitted to each of 1024 columns of an image near the interface (40 pixels per column). For each column, the location of the interface is identified where the fitted curve has the maximum intensity and it is averaged over 1024 samples. A typical value of the standard deviation is about 3 pixels (0.07 mm), and is a little larger than the limit of the measurement error (1 pixel). On the other hand, the theoretical interfacial displacement can be obtained by integrating the kinematic condition. In figure 3, we show both theoretical estimations and experimental measurements for the dimensionless variable $\zeta_m = \zeta_m'/H_0'$. The agreement between the measurements and theoretical predictions is very good. We also note that the displacements of the interface are almost three orders-of-magnitude smaller than

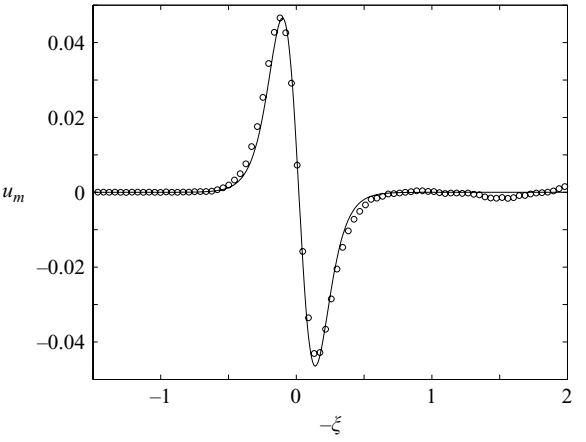

FIGURE 4. Time histories of the dimensionless horizontal velocity at $\eta = -0.5\overline{d}$ for $\epsilon = 0.190$; ——, the analytical solution; ○, the experimental data.

those of the free surface. Thus, the effect of the interface displacements can be safely neglected when the viscosity ratio is much greater than 1.

4.3. *Velocity field inside the mud layer*

The time history of the horizontal velocity at $\eta = -0.5\overline{d}$ for $\epsilon = 0.190$ is shown in figure 4. Again, the theoretical results agree very well with the experimental measurements and similar excellent agreement is found in the other two cases. The integrals in the analytical solution (2.5) are numerically evaluated using Simpson quadrature. Twenty terms in the series are used, although the solution has already converged when ten terms are used.

In all experiments conducted, $\overline{d}$ is less than 0.2 (see table 1), i.e. the mud bed thickness is less than 20 % of the wave-induced boundary-layer thickness. The vertical profiles of horizontal velocity components at four different phases are plotted in figure 5(*a–d*). Indeed, in this case, the velocity profiles can be fitted approximately as a parabolic function as follows:

$$u_m \approx -\frac{\gamma}{2}\frac{\partial u_b}{\partial t}(\eta^2 - \overline{d}^2). \tag{4.1}$$

Note that (4.1) has been found by requiring a parabolic solution form to satisfy the depth-averaged horizontal momentum equation as well as the no-slip condition at the bottom of the mud bed ($\eta = -\overline{d}$) and the shear-stress-free condition along the water–mud interface ($\eta = 0$). On the other hand, if $\overline{d}$ is greater than unity, the parabolic approximation is no longer valid and flow reversal near the bottom will occur during the deceleration phase ($-\xi > 0$). For example, in figure 5(*e–h*) the analytical solutions are shown for the same conditions as those used in figure 5(*a–d*) except that $\overline{d}$ is increased to 2.

When the thickness of the mud bed is further increased such that it is much greater than the boundary-layer thickness, a boundary-layer flow region is developed under a 'plug flow' region where the velocity is uniform (shear-free). This feature can be seen in figure 5(*i–p*), i.e. for $\overline{d} = 5$ and 10. In the plug flow region, the inertia force is balanced by the pressure gradient force. Therefore, the plug flow velocity can be determined as $u_p = \gamma u_b$. A contour plot of $\partial u_m/\partial\eta$ is shown in figure 6 for $\overline{d} = 10$ and $\epsilon = 0.190$. In the plug flow region, the value of the derivative should be very close to

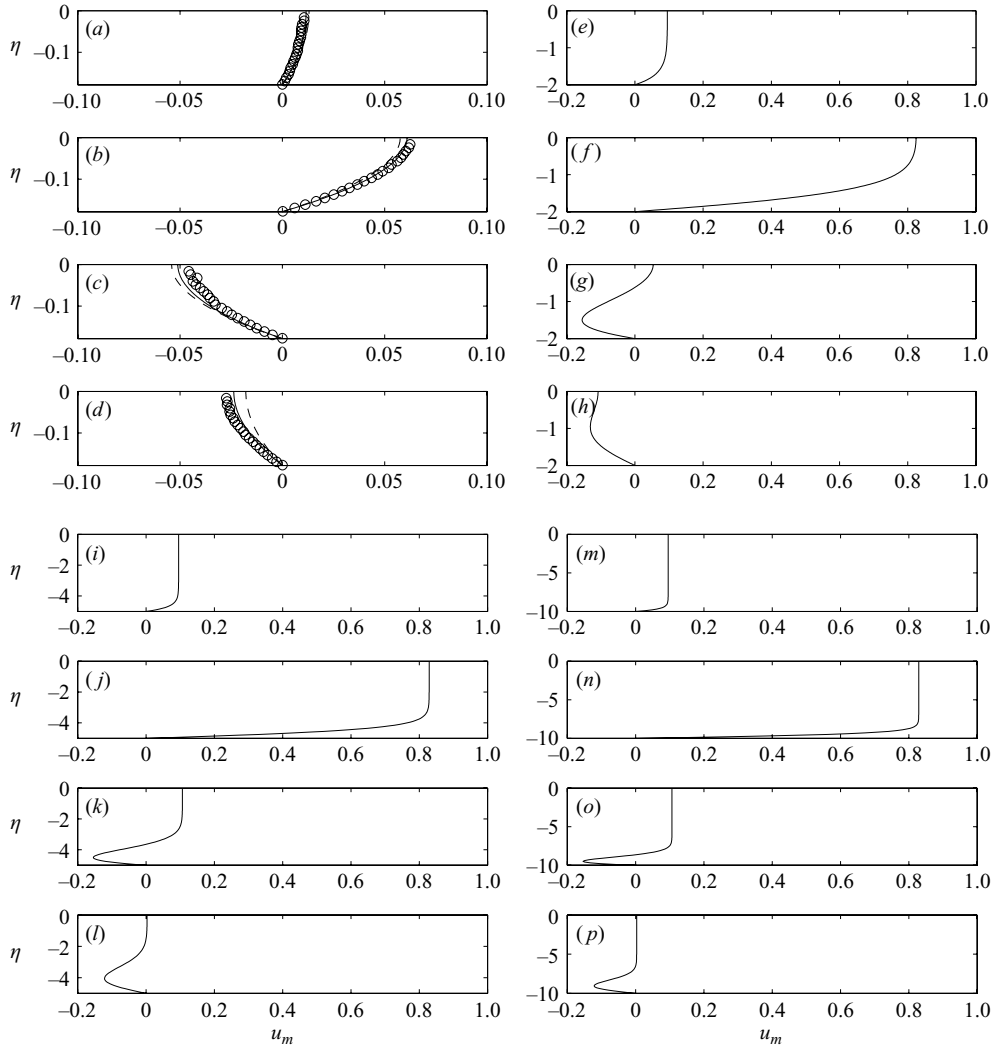

FIGURE 5. Vertical profiles of the dimensionless horizontal velocity at different phases for $\epsilon = 0.190$ for $\overline{d} = 0.178$ (*a–d*), $\overline{d} = 2$ (*e–h*), $\overline{d} = 5$ (*i–l*) and $\overline{d} = 10$ (*m–p*): ——, the analytical solution; – – –, the parabolic approximation; ○, the experimental data. (*a*) $-\xi = -0.33$; (*b*) $-\xi = -0.12$; (*c*) $-\xi = 0.09$; (*d*) $-\xi = 0.33$; (*e*, *i*, *m*) $-\xi = -0.3$; (*f*, *j*, *n*) $-\xi = 0.0$; (*g*, *k*, *o*) $-\xi = 0.3$; (*h*, *l*, *p*) $-\xi = 0.6$.

zero. If we define the bottom of the plug flow as the location where $\partial u_m/\partial\eta = \pm 0.2$, figure 6 provides the evolution of the plug flow thickness as the solitary wave passes by.

4.4. *Bottom shear stress*

The dimensionless bottom shear stress for $\epsilon = 0.190$ is shown in figure 7. The experimental results are obtained by least-squares fitting a straight line through 10 data points (within 1 mm) above the bottom of the mud bed, whereas the theoretical values are calculated from (2.6). Again agreement is excellent. Note that the time history of the bottom shear stress is almost symmetric with respect to zero stress, for the experimental case.

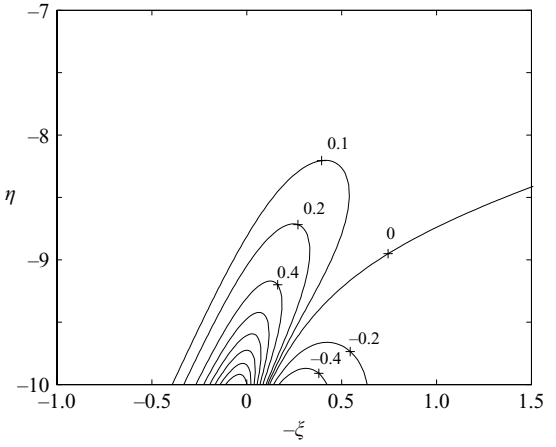

FIGURE 6. A contour plot of $\partial u_m/\partial\eta$ when $\overline{d} = 10$ for the case of $\epsilon = 0.190$.

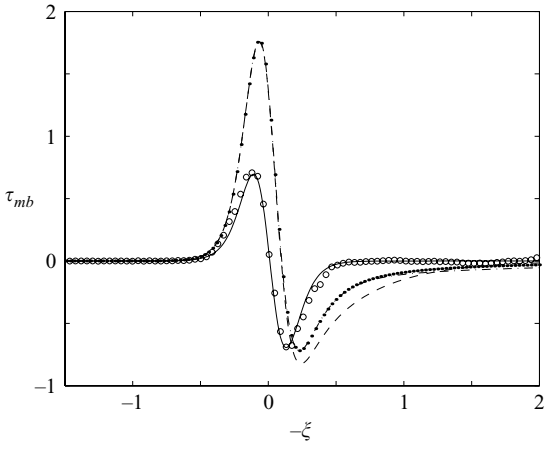

FIGURE 7. Time histories of the dimensionless bottom shear stresses for $\epsilon = 0.190$: ○, the experimental data for $\overline{d} = 0.178$; ——, the analytical solution (2.6) for $\overline{d} = 0.178$; – – –, the analytical solution for $\overline{d} = 1$; — · —, for $\overline{d} = 2$; •, for $\overline{d} = 5$.

Also plotted in the same figure are bottom shear stresses for different values of $\overline{d}$ with otherwise identical conditions. They are no longer symmetric with respect to zero stress, as a distinct shear layer is developed inside the mud bed and the phase difference from that of the forcing wave is apparent. It is also clear that the bottom shear stress becomes independent of the mud bed thickness when $\overline{d}$ exceeds a critical value, which can be determined from the analytical solutions. For the case of $\epsilon = 0.190$, the critical value is roughly $\overline{d} \approx 1.5$.

5. Concluding remarks

We have presented theoretical and experimental analyses on the viscous flows inside a muddy seabed which is driven by the horizontal pressure gradient induced by a solitary wave. Analytical solutions suggested by LC have been compared with PIV experiments. The PIV experiments were carried out for the case in which the thickness of the mud layer is smaller than that of the bottom boundary layer of the viscous mud,

i.e. $\overline{d} < 1$. First, the interface displacements are predicted by requiring a kinematic condition at the interface, which agreed well with the measurements. Time histories of the horizontal velocity showed that velocities at different elevations have the same direction when $\overline{d} < 1$ and the velocity profile can be fitted by a parabola. However, when the thickness of the mud layer is much larger than the bottom boundary-layer thickness, the velocity profile appears to be a plug flow above a thin viscous layer. The plug flow velocity and thickness can be determined theoretically. More complex flows occur for $\overline{d} \sim O(1)$. Finally, measured and estimated time histories of the bottom shear stress show that it becomes almost independent of $\overline{d}$, when $\overline{d} > 1.5$.

This work has been supported by grants from the National Science Foundation and the Office of Naval Research to Cornell University. Y. S. P. would also like to acknowledge the support from Korea Science and Engineering Foundation under grant M06-2004-000-10541. Finally, the authors wish to thank N. W. Choi for suggesting the highly viscous silicone fluid used in the experiments.

REFERENCES

Dalrymple, R. A. & Liu, P. L.-F. 1978 Waves over soft mud: a two-layer fluid model. *J. Phys. Oceanogr.* **8**, 1121–1131.

Foda, M. A. 1989 Sideband damping of water waves over a soft bed. *J. Fluid Mech.* **201**, 189–201.

Gade, H. G. 1958 Effects of non-rigid, impermeable bottom on plane surface waves in shallow water. *J. Mar. Res.* **16**, 61–82.

Grimshaw, R. 1971 The solitary wave in water of variable depth. Part 2. *J. Fluid Mech.* **46**, 611–622.

Liu, P. L.-F. 1973 Damping of water waves over porous bed. *J. Hydraul. Div. ASCE* **99**, 2263–2271.

Liu, P. L.-F. & Chan, I.-C. 2007 On long wave propagation over a fluid-mud seabed. *J. Fluid Mech.* **579**, 467–480.

Liu, P. L.-F. & Orfila, A. 2004 Viscous effects on transient long-wave propagation. *J. Fluid Mech.* **520**, 83–92.

Liu, P. L.-F., Park, Y. S. & Cowen, E. A. 2007*a* Boundary layer flow and bed shear stress under a solitary wave. *J. Fluid Mech.* **574**, 449–463.

Liu, P. L.-F., Park, Y. S. & Lara, J. L. 2007*b* Long-wave-induced flows in an unsaturated permeable seabed. *J. Fluid Mech.* **586**, 323–345.

MacPherson, H. 1980 The attenuation of water waves over a non-rigid bed. *J. Fluid Mech.* **97**, 721–742.

Wen, J. & Liu, P. L.-F. 1995 Mass transport in water waves over an elastic bed. *Proc. R. Soc. Lond.* A **450**, 371–390.

Yamamoto, T., Koning, H. L., Sellmeijer, H. & Hijum, E. V. 1978 On the response of a poro-elastic bed to water waves. *J. Fluid Mech.* **87**, 193–206.